Scattering from Planar Structures Containing Small Features Using the Adaptive Integral Method (AIM)

Sunil S. Bindiganavale, John L. Volakis, *Fellow, IEEE*, and Hristos Anastassiu, *Member, IEEE*

***Abstract*—Fast integral equation algorithms such as the adaptive integral method (AIM) have been demonstrated to reduce memory and execution time associated with moment-method solutions for arbitrarily shaped three-dimensional (3-D) geometries. In this paper, we examine the efficiency of AIM in modeling planar structures that contain small and intricate details as is the case with spirals and slot antennas. Such geometries require high tessellation due to the inclusion of very small features resulting in a large number of unknowns. AIM with its capability to translate the original grid to an equivalent sparser uniform grid is uniquely suited for the analysis of such geometries. In the latter part of the paper, we demonstrate the application of AIM in connection with a finite-element boundary-integral formulation for cavity-backed antennas.**

***Index Terms*—Adaptive integral method, antennas, fast integral equation solvers, scattering.**

I. Introduction

FAST integral-equation methods were introduced in the early 1990's and have been shown effective in accelerating the computation of matrix–vector products required by iterative solvers. The adaptive integral method (AIM) [1] and fast multipole method (FMM) [2] belong to this class of fast integral-solution techniques. Other fast integral methods (that can be considered as variations of AIM and FMM) have been considered in [3] and [4]. However, these latter methods have only been developed and applied to static field solutions. In contrast, [1] and [2] refer to three-dimensional (3-D) solutions of time-harmonic fields. Both AIM and FMM reduce the solution time and memory requirements of the moment method (MM), and their initial applications focused on scattering from large conducting bodies. More recently, FMM has been employed successfully in hybrid methods [5], [6] to evaluate scattering from composite structures.

AIM achieves its central processing unit (CPU) and memory reduction by mapping the original multipole method (MM) discretization onto a rectangular grid and then exploiting the Toeplitz property of the Green's function on this grid; that is, the fast Fourier transform (FFT) is invoked to compute the matrix–vector products in the iterative solver. For an arbitrary 3-D body, a 3-D FFT is required and, as can be understood, this calculation is very time consuming. For planar applications of the method, the dimensionality of the FFT is reduced by one, thereby significantly accelerating the solution. In this paper, we present the AIM formulation specialized to planar geometries with particular emphasis on exploring the method's efficiency in dealing with highly tessellated geometries as is the case with surfaces containing small but important features. Examples include slot and spiral antennas. While other fast integral-equation algorithms employ the same dense grid, the overlaid AIM uniform grid allows use of sparser grids. This leads to far fewer boundary integral unknowns, in addition to CPU and memory gains inherent with the AIM implementation. After presenting the AIM formulation specialized to planar surfaces, results are given that examine the accuracy for near- and far-field calculations when sparser AIM grids are employed. Five plate geometries (containing various narrow slots and fine features) are examined to evaluate AIM's speed up and memory reductions. Three antenna configurations are also analyzed in the context of the finite-element boundary-integral (FE-BI) method where AIM is employed to reduce memory requirement and speed up the calculation of the boundary integral matrix–vector products.

Manuscript received March 3, 1997; revised May 6, 1998.

The authors are with the Radiation Laboratory, Department of Electrical Engineering and Computer Science, The University of Michigan, Ann Arbor, MI 48109 USA.

Publisher Item Identifier S 0018-926X(98)09714-2.

II. AIM for Planar Surfaces

The AIM algorithm for arbitrary 3-D bodies has been given in [1]. In this section, we describe its specialization to planar geometries, giving only the essential details required for its implementation. Consider a planar arbitrary conducting body whose surface S is illuminated by an incident plane wave $\boldsymbol{E}^i$. The boundary condition enforced on S is (e^{jwt} time convention is employed)

$$(\boldsymbol{E}^i + \boldsymbol{E}^s) \cdot \hat{t} = 0 \tag{1}$$

where the scattered field $\boldsymbol{E}^s$ is given by

$$\boldsymbol{E}^s = -j\omega \boldsymbol{A} - \nabla \phi \tag{2}$$

in which

$$\boldsymbol{A}(\boldsymbol{r}) = \frac{\mu}{4\pi} \int_S \boldsymbol{J}_s(\boldsymbol{r}') \frac{e^{-jkR}}{R}\, dS' \tag{3}$$

is the vector potential and

$$\phi(\boldsymbol{r}) = \frac{j}{4\pi\omega\epsilon} \int_S \nabla_S \cdot \boldsymbol{J}_s(\boldsymbol{r}') \frac{e^{-jkR}}{R}\, dS' \tag{4}$$

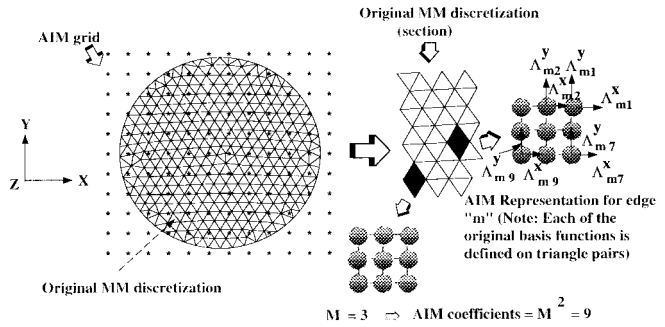

Fig. 1. The process of transformation from the original MM grid onto the AIM grid.

is the scalar potential. Substituting (2)–(4) into (1) gives the necessary integral equation, which must be discretized for the solution of $\boldsymbol{J}_s$. To do so, the equivalent electric current density $\boldsymbol{J}_s$ is expanded using linear basis functions [7] as

$$\boldsymbol{J}_s(\boldsymbol{r}') = \sum_N I_n \boldsymbol{f}_n(\boldsymbol{r}') \tag{5}$$

where I_n are the unknown coefficients. Application of Galerkin's technique leads to the linear system

$$[Z]\{I\} = \{V\} \tag{6}$$

with $[Z]$ being the elements interaction matrix whereas $\{I\}$ is the vector of the unknown coefficients and $\{V\}$ is the excitation vector. The matrix $[Z]$ is fully populated, demanding $O(N^2)$ storage, and each $[Z]\{I\}$ matrix–vector product requires $O(N^2)$ multiplications.

Fast algorithms such as FMM and AIM are used to reduce the operation count from N^2 down to N^α, where $\alpha \leq 1.5$. Both algorithms work on approximating the far-zone interactions. In the case of AIM, the CPU reduction is achieved by first splitting the matrix as

$$[Z] = [Z^{\text{near}}] + [Z^{\text{far}}] \tag{7}$$

based on a threshold distance referred to as the near-zone radius. The matrix $[Z^{\text{near}}]$ contains the interactions between elements separated less than a threshold distance, whereas $[Z^{\text{far}}]$ contains the remaining interactions. The elements of $[Z^{\text{near}}]$ are evaluated with the exact MM while those of $[Z^{\text{far}}]$ and the product $[Z^{\text{far}}]\{I\}$ are evaluated in an approximate manner as prescribed by the AIM procedure [1].

Application of AIM requires that the whole geometry be enclosed in a regular rectangular grid. However, for planar geometries, it is only necessary to employ a planar uniform grid that can be coincident with the original triangular grid. Equivalent point sources are placed at each node whose strength is dictated by matching multipole moments of the basis functions between the original and uniform grids. Basically, the field of each interior edge is re-expressed using a new expansion involving delta sources located at the nodes of the uniform AIM grid as depicted in Fig. 1. For the mth edge, this new expansion has the form

$$\overline{\psi}_m = \sum_{q=1}^{M^2} \delta(x - x_{mq})\delta(y - y_{mq})[\Lambda_{mq}^x \hat{x} + \Lambda_{mq}^y \hat{y}] \tag{8}$$

where $\boldsymbol{r}_{mq}$ are the position vectors of M^2 points on the square surrounding the center of the edge and $\delta(x)$ is the usual Dirac delta function. The coefficients $\Lambda_m^{x,y}$ are suitably chosen so that the new expansion is equivalent to the original representation using triangular elements with respect to generating identical far field. A similar expansion is used for the divergence of the basis functions

$$\psi_m^d = \sum_{q=1}^{M^2} \delta(x - x_{mq})\delta(y - y_{mq})\Lambda_{mq}^d. \tag{9}$$

To find a relation between the $\Lambda_m^{x,y}$ and I_n coefficients, we equate moments of the two expansions up to order M. Specifically, we set

$$\boldsymbol{M}_{q_1,q_2}^m = \boldsymbol{F}_{q_1,q_2}^m \tag{10}$$

where

$$\begin{aligned}\boldsymbol{M}_{q_1,q_2}^m &= \int_{-\infty}^{\infty}\int_{-\infty}^{\infty} \overline{\psi}_m (x - x_a)^{q_1}(y - y_a)^{q_2}\, dx\, dy \\ &\qquad \text{for } 0 \leq q_1, q_2 \leq M \\ &= \sum_{q=1}^{M^2} (x_{mq} - x_a)^{q_1}(y_{mq} - y_a)^{q_2}[\Lambda_{mq}^x \hat{x} + \Lambda_{mq}^y \hat{y}] \\ &\qquad \text{with } q = q_1 + q_2 \end{aligned} \tag{11}$$

$$\boldsymbol{F}_{q_1,q_2}^m = \int_{-\infty}^{\infty}\int_{-\infty}^{\infty} \boldsymbol{f}_m (x - x_a)^{q_1}(y - y_a)^{q_2}\, dx\, dy \tag{12}$$

with (x_a, y_a) being the coordinates of the center of the edge. Similarly, by equating moments of $\nabla_s \cdot \boldsymbol{J}_s$ with the new expansion (9), we establish a relation between Λ_m^d and I_n; that is, we set

$$D_{q1,q2}^m = H_{q1,q2}^m \tag{13}$$

where

$$\begin{aligned} D_{q_1 q_2}^m &= \int_{-\infty}^{\infty}\int_{-\infty}^{\infty} \psi_m^d (x - x_a)^{q_1}(y - y_a)^{q_2}\, dx\, dy \\ &= \sum_{q=1}^{M^2} (x_{mq} - x_a)^{q_1}(y_{mq} - y_a)^{q_2} \Lambda_{mq}^d \end{aligned} \tag{14}$$

$$H_{q_1 q_2}^m = \int_{-\infty}^{\infty}\int_{-\infty}^{\infty} (x - x_a)^{q_1}(y - y_a)^{q_2} \nabla_s \cdot \boldsymbol{f}_m\, dx\, dy. \tag{15}$$

Equations (10) and (13) give three $M^2 \times M^2$ systems yielding the equivalence coefficients as the solution. This process is depicted pictorially in Fig. 1.

Were we to use the equivalent expansions to represent the currents everywhere, the resulting impedance matrix will be of the form

$$[Z_{\text{AIM}}^{\text{total}}] = \sum_{i=1}^{3} [\Lambda]_i [G] [\Lambda]_i^T. \tag{16}$$

In this, $[\Lambda]_i$ are the sparse matrices containing the coefficients of the expansion (11) and (9), whereas $[G]$ is the Toeplitz matrix whose elements are the free-space Green's function evaluated at the grid points. It has been shown in [1] that

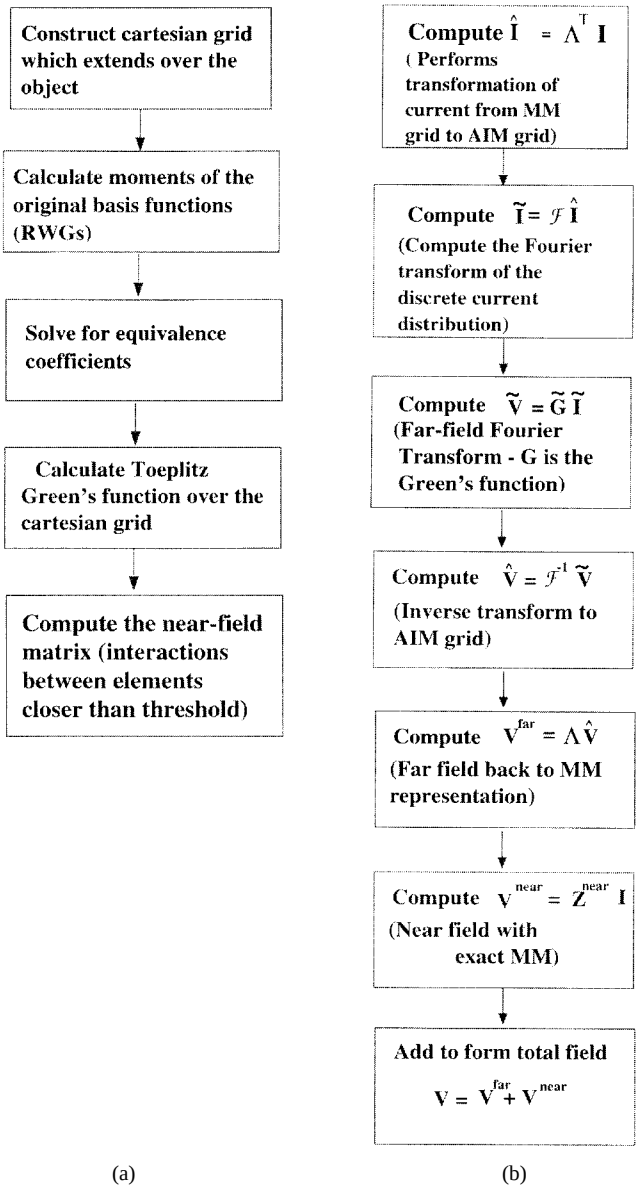

Fig. 2. (a) Matrix-built operations. (b) Matrix–vector product computation in AIM.

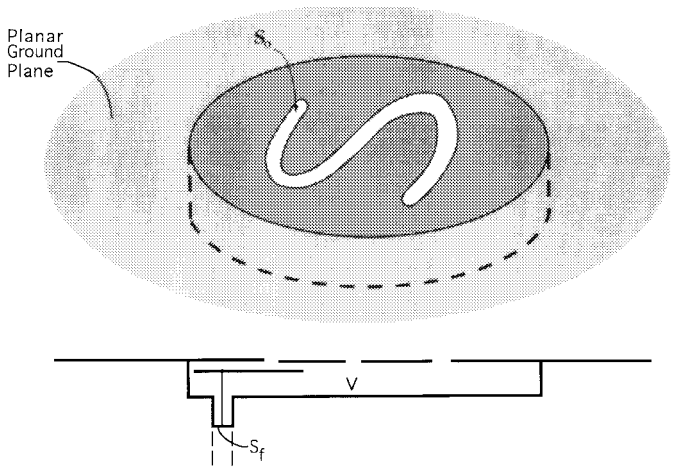

Fig. 3. Geometry of a cavity-backed annular slot antenna in a ground plane.

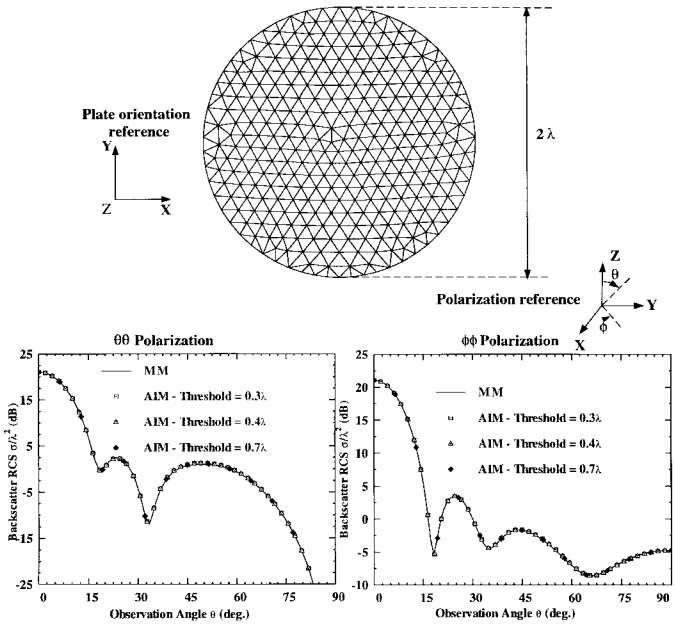

Fig. 4. Monostatic RCS for a circular plate of diameter 2λ. Comparison of the standard MM and AIM.

$[Z_{\rm AIM}^{\rm total}]$ is not of sufficient accuracy for modeling the interactions between the nearby current elements. To take advantage of the Toeplitz structure of $[G]$ and sparsity of $[\Lambda]$ we can still use $[Z_{\rm AIM}^{\rm total}]$ to represent the far element interactions. However, we will retain the exact interaction matrix elements for the near element interactions; that is, we rewrite $[Z_{\rm AIM}^{\rm total}]$ as

$$[Z_{\rm AIM}^{\rm total}] = [Z_{\rm AIM}^{\rm near}] + [Z_{\rm AIM}^{\rm far}]. \tag{17}$$

Comparing this to (7) and setting $[Z^{\rm far}] \simeq [Z_{\rm AIM}^{\rm far}]$ we can rewrite the original $[Z]$ matrix as

$$[Z] \simeq ([Z^{\rm near}] - [Z_{\rm AIM}^{\rm near}]) + [Z_{\rm AIM}^{\rm total}] \tag{18}$$

or

$$[Z] \simeq [S] + \sum_{i=1}^{3} [\Lambda]_i [G] [\Lambda]_i^T \tag{19}$$

where $[S] = [Z^{\rm near}] - [Z_{\rm AIM}^{\rm near}]$ is a sparse matrix corresponding to the difference between the near-field interactions computed by MM and AIM. The Toeplitz property of the Green's function defined on the regular grid enables use of the FFT to accelerate the computation of the matrix–vector product. The sequence of operations involved in the construction of the coefficient and Green's function matrices are indicated in Fig. 2(a); those for the matrix–vector product execution are outlined in Fig. 2(b).

III. Extension to Planar Cavity-Backed Antennas

Consider now a cavity-backed antenna recessed in a ground plane as depicted in Fig. 3. This class of configurations have been modeled using the finite element [8]–[10] very successfully. The most rigorous of the implementations is to employ the finite-element method to model the interior volume below the cavity and the boundary integral for truncating the

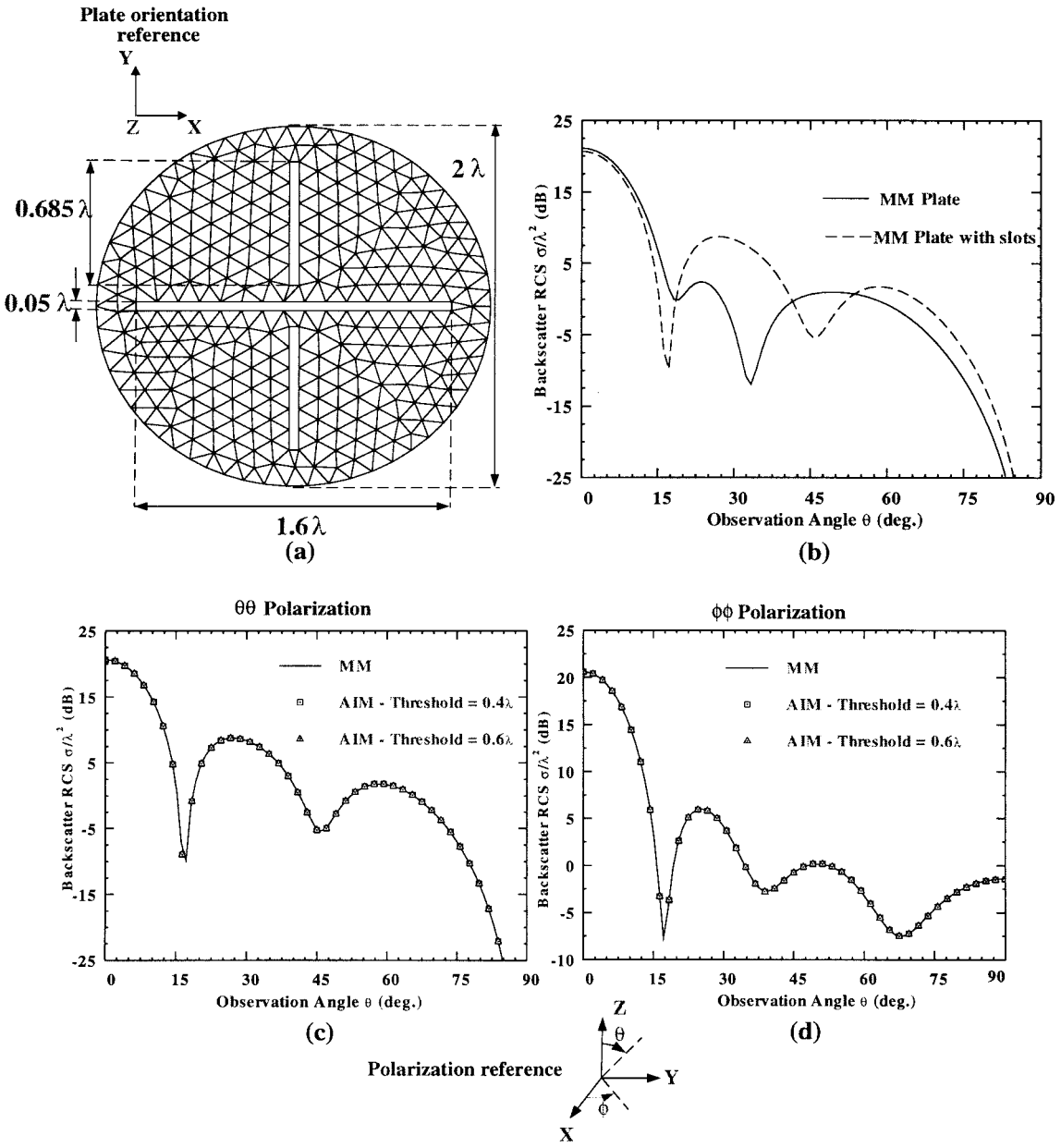

Fig. 5. Monostatic RCS for a circular plate of diameter 2λ with three slots computed with standard MM and AIM. (a) Geometry. (b) Effect of the slots on the RCS. (c) $\theta\theta$ polarization backscatter RCS for the plate with slots. (d) $\phi\phi$ polarization backscatter RCS for the plate with slots.

finite-element mesh on the antenna/cavity aperture [8], [9]. As expected, for large apertures the CPU and memory requirements are dominated by the boundary integral unknowns. This situation is exacerbated for narrow slot antennas where high tessellation is needed. Application of AIM for computing the boundary-integral matrix–vector products is, therefore, an important step toward reducing memory and CPU.

For a finite element–boundary integral simulation of the geometry in Fig. 3, the resulting system has the general form

$$[\mathcal{A}]\begin{Bmatrix}\{E^V\}\\ \{E^S\}\end{Bmatrix}+\begin{bmatrix}[0] & [0]\\ [0] & [\mathcal{B}]\end{bmatrix}\begin{Bmatrix}\{E^V\}\\ \{E^S\}\end{Bmatrix}=\begin{Bmatrix}\{b^V\}\\ \{b^S\}\end{Bmatrix} \quad (20)$$

where $\{E^V\}$ denotes the field unknowns within the volume enclosed by S_o whereas $\{E^S\}$ represents the corresponding unknowns on the boundary S_o. The excitation column $\{b^V\}$ is associated with interior (antenna) sources whereas $\{b^S\}$ is associated with incident-field excitations (for scattering). The entries for the sparse finite element matrix $[\mathcal{A}]$ are

$$A^e_{ij}=\iiint_{V_e}\{(\nabla\times\boldsymbol{W}_i)\cdot\overline{\overline{\mu_r}}^{-1}\cdot(\nabla\times\boldsymbol{W}_j) - k_0^2\boldsymbol{W}_i\cdot\overline{\overline{\epsilon_r}}\cdot\boldsymbol{W}_j\}\,dV \quad (21)$$

and those for the boundary-integral matrix are given by

$$B^s_{ij}=-\iint_{S_s}\iint_{S'_s}2k_0^2\boldsymbol{f}^s_i(\boldsymbol{r})\cdot\boldsymbol{f}^s_j(\boldsymbol{r}')G_0(\boldsymbol{r},\boldsymbol{r}')\,dS\,dS' + 2\iint_{S_s}\iint_{S'_s}\nabla\cdot[\boldsymbol{f}_i(\boldsymbol{r})\times\hat{z}]\nabla' \cdot[\boldsymbol{f}_j(\boldsymbol{r}')\times\hat{z}]G_0(\boldsymbol{r},\boldsymbol{r}')\,dS\,dS'. \quad (22)$$

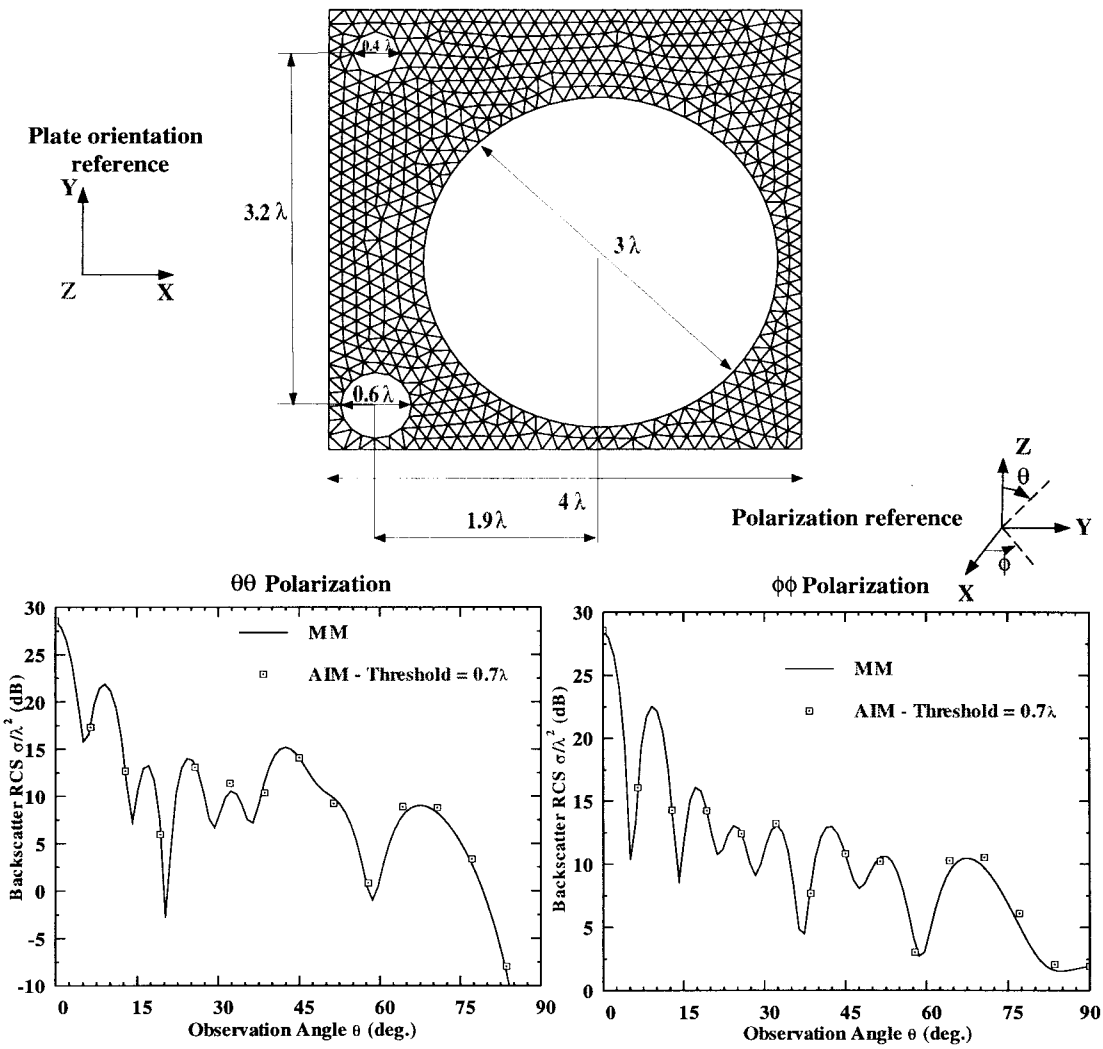

Fig. 6. Monostatic RCS for a circular plate of diameter 3 λ with three holes computed with standard MM and AIM.

Note that $\boldsymbol{W}_i$ refer to the edge-based basis [9], [10] and $\boldsymbol{f}_i$ are the Rao–Wilton–Glisson (RWG) basis [7]. Of importance is that B_{ij} are the same integrals as those resulting from enforcing (1) in conjunction with (2)–(5). The matrix–vector products can, therefore, be evaluated as discussed in the previous section using $O(N_S)$ memory and $O(N_S \log N_S)$ complexity ($N_S =$ number of aperture unknowns).

IV. Results and Parameter Investigation

When examining the merits of a fast integral algorithm such as AIM, of importance is the memory and CPU requirements, both contrasted to the delivered accuracy. Although approximate analytical expressions have been derived in [1] for some of these parameters, these refer to implementations involving cubical grids and the 3-D FFT. Our goal in this paper is to assess the accuracy of AIM in treating small details within an aperture/surface and to provide the reader with quantitative measures on the performance of AIM when implemented with the two-dimensional (2-D) FFT. The near-zone radius or threshold distance has a dramatic impact on the CPU requirements since it controls the nonzero element population of the system matrix. In the case of AIM, because of the inherent mapping to a different grid, we are highly interested in examining its suitability to model small and fine details embedded in much larger scale structures. The calculations for plate configurations given next are intended to address this issue by examining the method's performance for a number of representative and practical situations. All of the included results were generated using single precision arithmetic on an HP9000/C-110 workstation with a rated peak speed of 47 Mflops. In all cases, a third order $(M = 3)$ multipole expansion was used with a grid spacing of 0.05λ.

Figs. 4–8 depict the $\hat{\theta}\hat{\theta}$ and $\hat{\phi}\hat{\phi}$ polarization radar cross-section (RCS) patterns ($\phi = 0^0$ cut) as calculated by AIM for the different threshold distances indicated on the figures. The first circular plate (shown in Fig. 4) has no holes and was used to validate the method. From the pattern comparisons, it is clear that AIM recovers the exact result very well. As given in Tables I and II, AIM achieves this with at least a factor of five less memory than the traditional MM, even though the geometries are still rather small to demonstrate the full impact of AIM. Also, Table II shows that a near-zone radius of 0.3 λ is sufficient to maintain good accuracy (below 1 dB in root mean square (rms) error [11]).

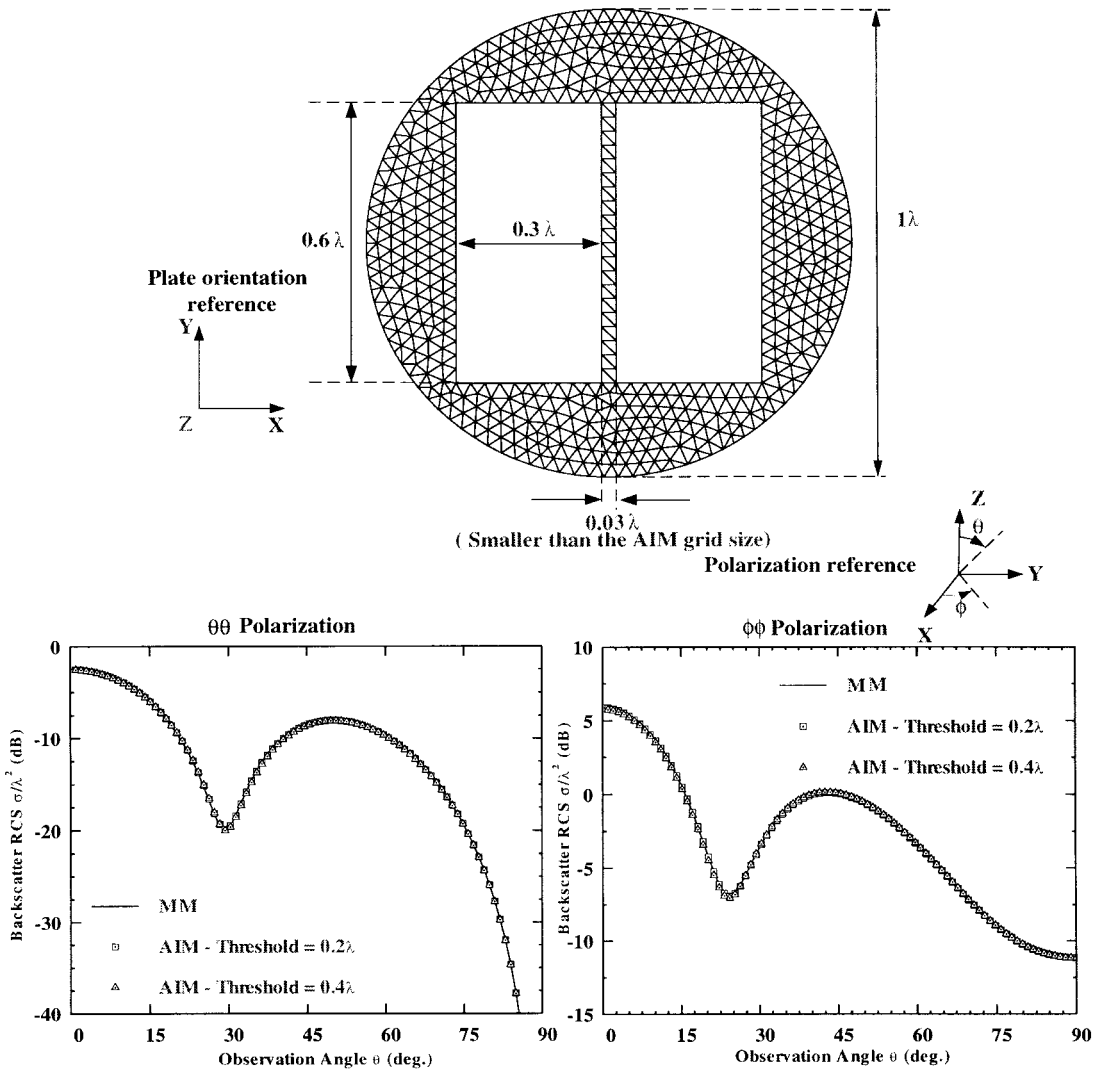

Fig. 7. Monostatic RCS for a circular plate of diameter 1 λ sampled at 0.03 λ (smaller than the AIM grid spacing) due to the narrow center ridge.

TABLE I
SOLUTION CPU TIME, MEMORY REQUIREMENT, AND RMS ERROR OF AIM (ALL ENTRIES IN THIS TABLE WERE COMPUTED WITH AN AIM GRID SPACING OF 0.05 λ)

Geometry	Discretization			MM memory (MB)	MM solution time
	Facets	Edges	Unknowns		$\hat{\theta}\hat{\theta}$ pol ($\theta = 0^0$ inc.)
Figure 4	586	908	850	5.51	32 secs
Figure 5	554	890	772	4.54	29 secs
Figure 6	1130	1806	1584	19.14	4 mins 50 secs
Figure 7	1036	1667	1441	15.84	4 mins
Figure 8	1038	1957	1157	10.21	2 mins 45 secs

TABLE II
SOLUTION CPU TIME, MEMORY REQUIREMENT, AND RMS ERROR OF AIM (ALL ENTRIES IN THIS TABLE WERE COMPUTED WITH AN AIM GRID SPACING OF 0.05 λ)

Geometry	AIM Data					
	Threshold	Non-Zeros	Memory	Solution time	RMS Error(dB)	
	(λ)	in Near Z	(MB)	$\hat{\theta}\hat{\theta}$ pol ($\theta = 0^0$ inc.)	$\hat{\theta}\hat{\theta}$ pol	$\hat{\phi}\hat{\phi}$ pol
Figure 4	0.3	59928	0.68	23 secs	0.1718	0.0755
	0.4	100182	1.14	25 secs	0.1490	0.0693
	0.7	257390	2.94	28 secs	0.0728	0.0490
Figure 5	0.4	79030	0.9	21 secs	0.0728	0.0583
	0.6	157994	1.8	27 secs	0.0721	0.0520
Figure 6	0.7	283774	3.24	3 mins 32 secs	0.8017	0.5185
Figure 7	0.2	296250	3.39	20 secs	0.1063	0.0949
	0.4	649556	7.43	31 secs	0.0548	0.0632
Figure 8	0.2	120220	1.37	18 secs	0.0469	0.0469

The advantage of AIM is more pronounced when gaps are inserted into the plate's surfaces and this is the primary reason that one may prefer AIM over other fast integral methods for planar structures. As depicted in Figs. 5 and 6, AIM maintains its accuracy for the same threshold criterion even though the gaps/slots have a dominant effect on the RCS pattern as shown in Fig. 5. In the case of narrow slots (or thin ridges in the plates) of width 0.03 λ, the memory requirements of the traditional MM increase quickly due to the higher element density. *For the geometry in Fig. 7, AIM yields a memory*

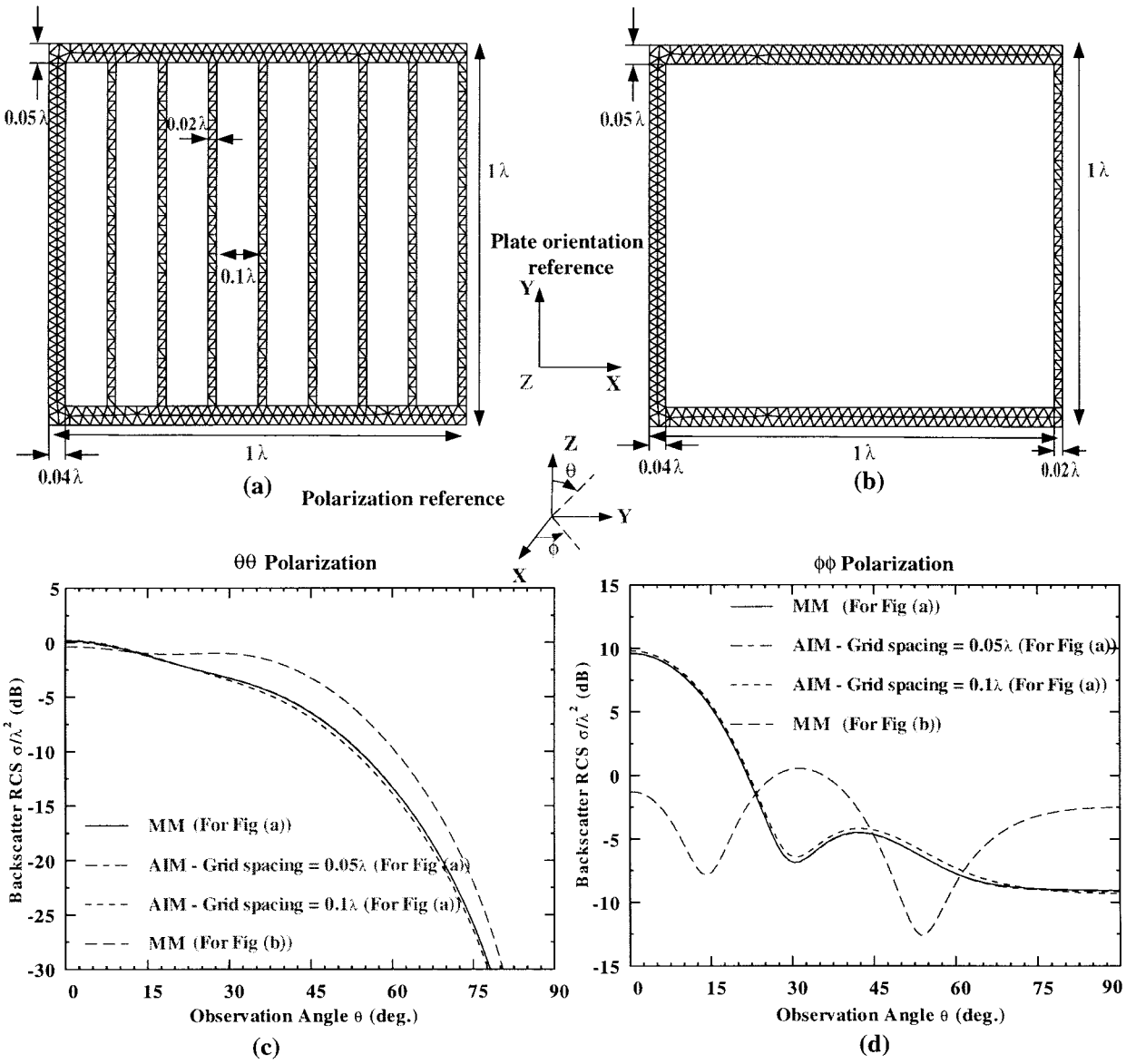

Fig. 8. (a) Geometry and mesh of the grated plate. (b) Geometry and mesh of the "groove" plate without gratings. (c) $\theta\theta$ polarization backscatter RCS computed by AIM and MM. (d) $\phi\phi$ polarization backscatter RCS computed by AIM and MM.

saving of 79% and the CPU time is reduced by a factor of 12 while retaining the monostatic pattern accuracy to within a tenth of a decibel. This is achieved by using a uniform AIM grid density of 20 points per linear wavelength even though the cell density of the original plate mesh is much greater due to the narrow slot. One may assume that this change in grid density will affect the near-zone field. However, our observations indicate that the surface current is equally accurate. For the configuration in Fig. 7 the average current density error is 7.3% for a threshold distance of 0.2 λ and 6% for a threshold distance of 0.4 λ. The currents for the geometry in Fig. 7 along the center narrow strip are plotted and compared in Fig. 9. These results demonstrate that the near-zone threshold criterion is not affected by the specific geometrical details, leading to tremendous memory savings. Moreover, the accuracy of the results provide a convincing argument that AIM can efficiently handle highly irregular and resonant (i.e., antenna) geometries as well as smooth scatterers. At the same time, the convergence rate of the AIM system is unaffected indicating that the system condition is unchanged. This is of critical importance for fast iterative solutions since an increase in the iteration count would annul the faster computation of the matrix–vector product.

Fig. 8 shows the monostatic RCS pattern for a grating structure that acts as a "polarization filter." The thin ridges in the grating cause a strong specular return for the $\hat{\phi}\hat{\phi}$ polarization (almost 10 dB above the return in the absence of the gratings) as is evident from the results in Fig. 8(d). Of importance is that the MM triangular mesh in Fig. 8 required a cell size of 0.02 λ per linear dimension because of the narrow grating. However, the overlaid rectangular AIM grid could be selected to have a much coarser discretization. More specifically, we chose grid spacings of 0.05 λ and 0.1 λ for the AIM grid and, thus, computational requirements of AIM were much lower. For the 0.1 λ grid spacing the solution time was reduced from 2.75 min down to only 12

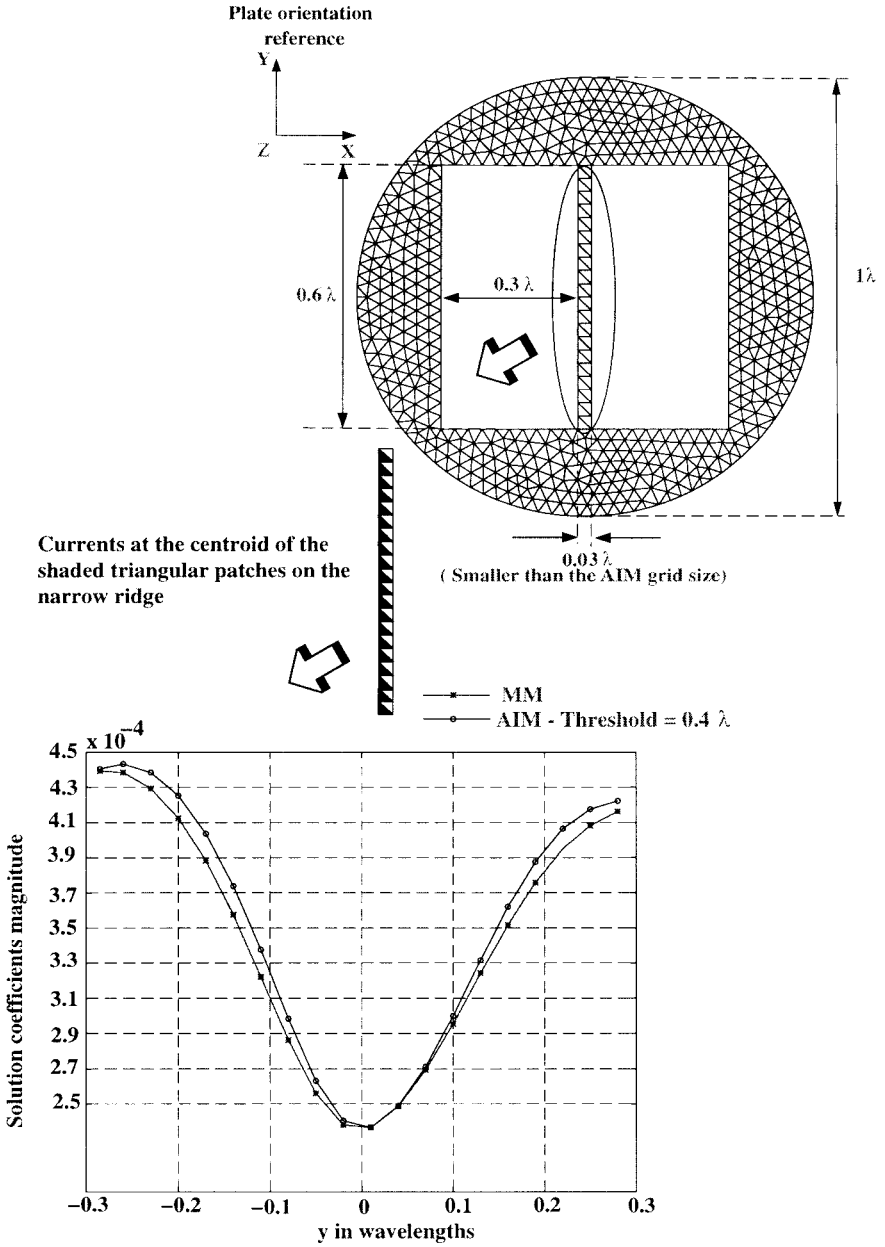

Fig. 9. Electric currents (solution coefficients) on the narrow ridge for the geometry of Fig. 7.

s at the expense of some accuracy (fraction of a decibel). To further increase in accuracy, we employed a 0.05 λ grid spacing and as shown in Fig. 8(b) the AIM curve is now indistinguishable from the reference MM result (within 0.1 dB). *From Tables I and II, the AIM computational and memory requirements are eight times and nine times less, respectively, without loss of accuracy*. This is a significant observation and we have found that both the convergence rate and condition of the AIM system remains essentially unchanged from the original moment-method system.

We next consider examples where AIM was used to speed-up computation of the boundary integral (BI) in the context of FE-BI for cavity-backed antenna modeling. The first step was to validate the spatial-domain FE-AIM formulation (i.e., the FE-BI formulation with AIM for implementing the BI matrix–vector products). To this end, Fig. 10 compares the FE-AIM solution with spectral-domain FE-BI data presented in [12] for scattering by a cavity-backed patch antenna. We next proceed to demonstrate memory savings and CPU time afforded by FE-AIM. Fig. 11 shows the radiation pattern in the $\phi = 90°$ elevation plane. The normal direction in this plane reveals the characteristic separation between copolarization and cross-polarization levels for the annular slot at observation angles close to normal in the elevation plane. From this figure it is gleaned that the threshold distance in AIM can be reduced down to even 0.15 λ if an average error of a decibels could be tolerated. From the computation of near-zone matrix entries such a threshold would result in a factor of five saving in memory.

A quantity of vital importance in antenna computations is the input impedance. Fig. 12 depicts the input impedance of a very narrow probe-fed annular slot computed using FE-

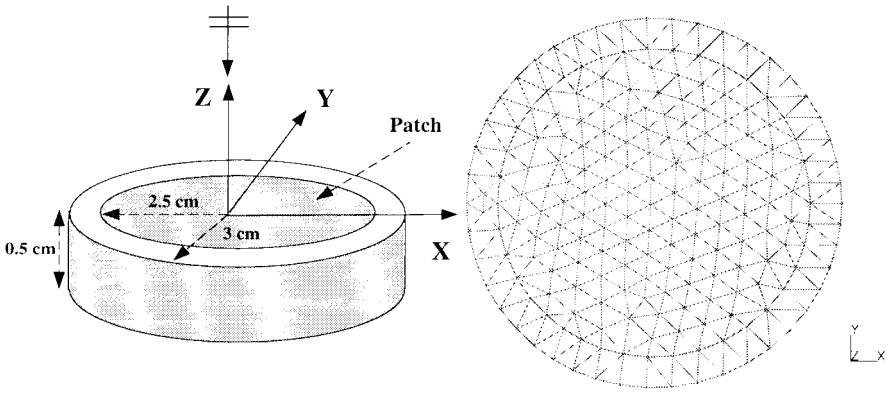

(a)

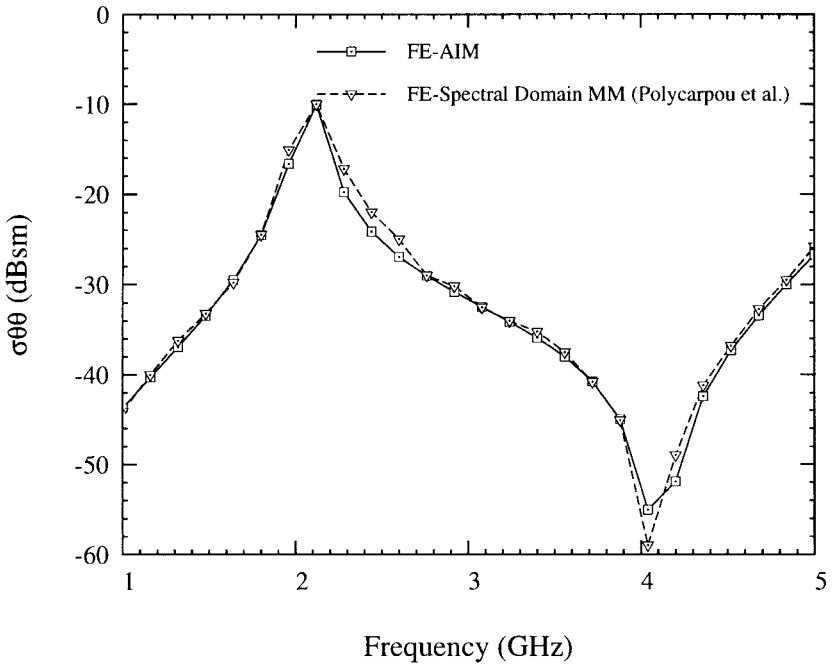

(b)

Fig. 10. (a) Geometry and surface discretization of a cavity-backed patch antenna. (b) Monostatic RCS at normal incidence versus frequency-cavity filling has a $\epsilon_r = 2.2 - j0.002$ and $\mu_r = 1$.

BI and FE-AIM. The probe is placed at $y = 0$ and we observe that the evaluation of the boundary integral with AIM enables the reduction of the near-zone nonzeros by more than half. Computation of the input impedance demands very high accuracy and the threshold distance was held constant at 10.5 cm (corresponding to 0.35 λ at 1 GHz and 0.49 λ at 1.4 GHz—the corresponding diameter of the entire BI contour varying from 0.513 λ to 0.718 λ).

Figs. 11 and 12 demonstrated how AIM leads to efficient BI computations by employing uniform grids rather than the original triangular tessellations. On the other hand, Fig. 13 indicates the importance of a low-threshold distance in modeling cavity-backed antenna arrays. It shows that for acceptable errors of less than 1 dB in scattering and radiation (radiation curves not shown) patterns, it is possible to reduce the number of nonzeros in the near-zone portion of the impedance matrix by a factor of six, resulting in substantial memory savings. This is a consequence of employing a threshold distance of 10 cm, i.e., about a fifth of the cavity diameter. Employing such a threshold distance results in a majority of the interactions between different slots being treated with the AIM procedure. This is of paramount importance in modeling slot arrays or other aperture antennas. Figs. 14 and 15 show the memory requirement and computational complexities for the implemented AIM algorithm. The plotted curves were obtained using actual data from the developed code. These curves along with the previous example computations lead to the following general conclusions.

- The rectangular AIM grid can be chosen to be much coarser than the original antenna grid. Thus, small antenna details do not drive the final degrees of freedom (DOF's) used for calculating the final matrix-vector products. Experience has shown that in computing far zone interactions (beyond 0.3 λ) the accuracy compromise in using nominal discretization (around 0.1 λ) is quite acceptable.
- For antenna applications, there is little or no wastage of grid points which may lie beyond the aperture when the

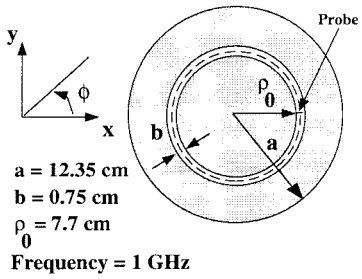

	Non-zeros in near Z matrix
FE-BI	4656
FE-AIM (0.15 λ)	915
FE-AIM (0.25 λ)	1537
FE-AIM (0.35 λ)	2245

	Average Error (dB)	
	Co-pol	X-pol
FE-AIM (0.15 λ)	1.0524	1.0373
FE-AIM (0.25 λ)	0.6142	0.9105
FE-AIM (0.35 λ)	0.876	0.2506

(a)

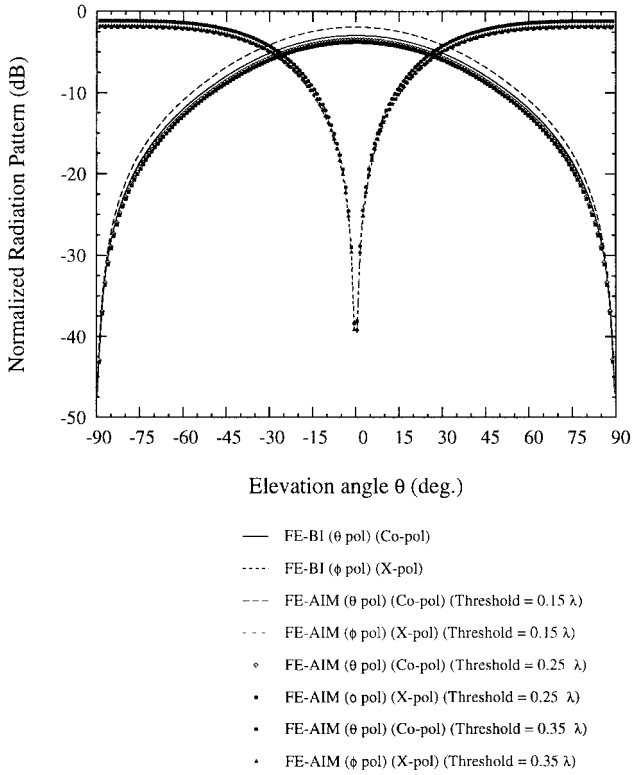

(b)

Fig. 11. Radiation pattern from an annular slot in the $\phi = 90^\circ$ elevation plane.

original grid is overlaid with the rectangular AIM grid. Thus, 2-D FFT's can be efficiently employed for calculating the matrix–vector products are done in [13]–[15].

- The near-zone matrix elements are calculated using the original boundary matrix and discrete elements. Thus, as in the case of FMM (but not so with the implementation in [16] and [17]), AIM makes no compromises in modeling the near-zone interactions. In the implementation of AIM this is achieved by decomposing the matrix into two matrices, one that contains the near zone interaction (a sparse matrix) and another that is a product of sparse and Toeplitz matrices and represents the interactions of the equivalent sources on the AIM rectangular grid.
- AIM leads to $O(N_S \log N_S)$ CPU requirements for the BI matrix–vector product evaluation as a consequence of the Toeplitz/Circulant nature of the boundary matrix associated with the uniform AIM grid. The corresponding memory requirements are of the same order or less and this holds even for small subsystems.

V. Summary

A memory reduction of 5–10 times over traditional MM was observed without noticeable compromise in accuracy when AIM is applied using a threshold radius of 0.2 λ. This CPU reduction is achieved without resorting to parallelization or optimization techniques (as is known, AIM is particularly amenable to such improvements). More importantly, AIM with coarser overlaid uniform grids is capable of modeling very small details in large bodies using considerably less memory while retaining a high degree of accuracy. This is of importance when modeling broad-band antennas (spirals or log periodics) and gratings, which are both large in overall size but can contain features as small as $\lambda/100$ in size.

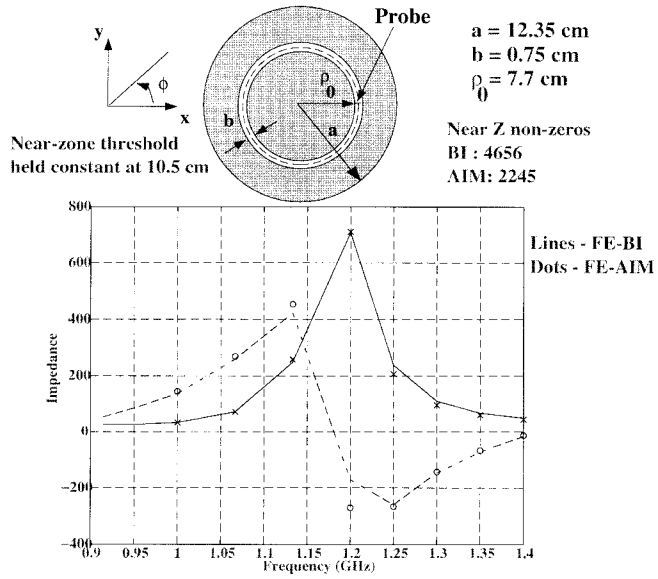

Frequency (GHz)	FE-BI	FE-AIM
1.0667	71.74 + j259.04	71.46 + j268.51
1.1333	248.51+j422.88	258.03 + j453.73
1.2	708.59-j170.31	710.39 - j269.71
1.25	238.47-j259.27	206.96 - j266.05
1.3	109.77-j146.96	95.48 - j142.82
1.35	67.63 - j71.61	59.84 - j 67.16
1.4	49.7 - j16.48	44.42-j12.95

Fig. 12. Input impedance of a very narrow annular slot computed with FE-BI and FE-AIM.

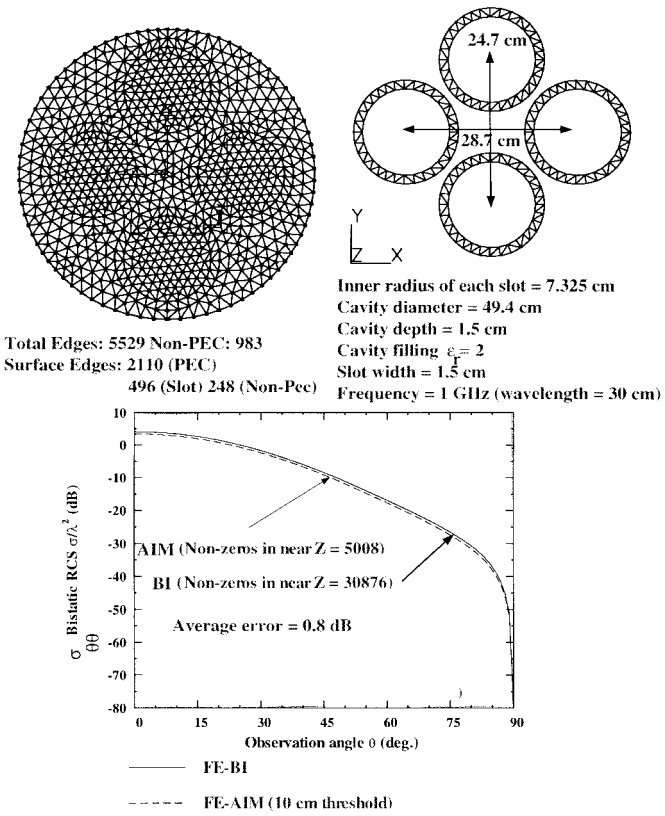

Fig. 13. Bistatic RCS at normal incidence ($\phi = 90^\circ$ plane) from a cavity-backed slot array computed with FE-BI and FE-AIM.

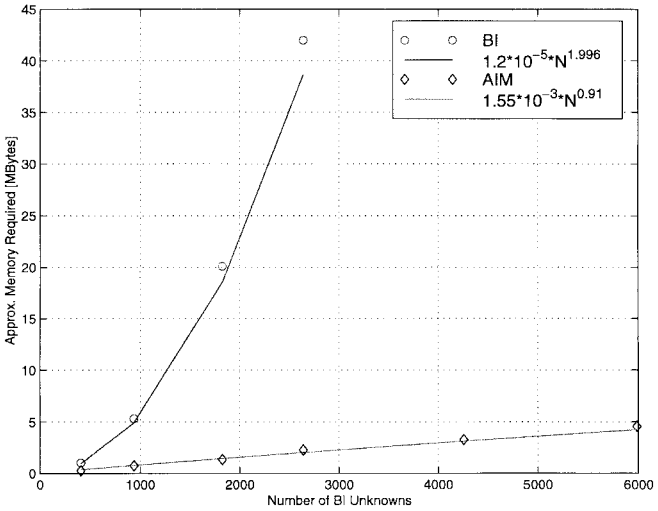

Fig. 14. Approximate memory required by the implemented AIM and BI algorithms; symbols refer to actual data and the solid line is an average curve through the actual data.

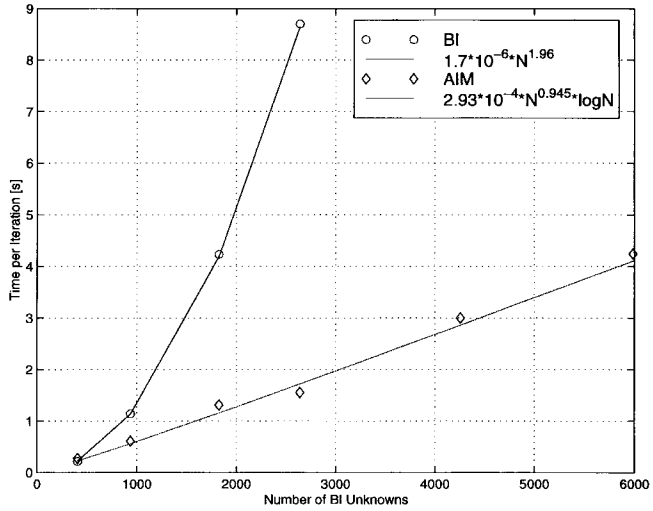

Fig. 15. Time per iteration complexity of the implemented BI and AIM algorithms; symbols refer to actual data and the solid lines are average curves through the actual data.

ACKNOWLEDGMENT

The authors would like to thank D. Filipovic for supplying the results for the algorithm complexities. They would also like to thank M. Bleszynski for discussions on various aspects of AIM and related implementations issues.

REFERENCES

[1] E. Bleszynski, M. Bleszynski, and T. Jaroszewicz, "AIM: Adaptive integral method for solving large-scale electromagnetic scattering and radiation problems," *Radio Sci.*, vol. 31, no. 5, pp. 1225–1251, 1996.

[2] V. Rokhlin, "Rapid solution of integral equations of scattering theory in two dimensions," *J. Computat. Phys.*, vol. 86, no. 2, pp. 414–439, 1990.

[3] J. R. Philips and J. K. White, "Efficient capacitance computation of 3D structures using generalized pre-corrected FFT method," in *Proc. 3rd Topical Meeting Elect. Performance Elect. Packaging*, 1994, pp. 253–256.

[4] S. D. Senturia, N. Aluru, and J. White, "Simulating the behavior of MEMS devices: Computational methods and needs," *IEEE Trans. Computat. Sci. Eng.*, vol. 4, pp. 30–43, Mar. 1997.

[5] S. S. Bindiganavale and J. L. Volakis, "A hybrid FEM-FMM technique for electromagnetic scattering," *IEEE Trans. Antennas Propagat.*, vol. 45, pp. 180–181, Jan. 1997.
[6] N. Lu and J. M. Jin, "Application of the fast multipole method to finite element-boundary integral solution of scattering problems," *IEEE Trans. Antennas Propagat.*, vol. 44, pp. 781–786, June 1996.
[7] S. M. Rao, D. R. Wilton, and A. W. Glisson, "Electromagnetic scattering by surfaces of arbitrary shape," *IEEE Trans. Antennas Propagat.*, vol. AP-30, pp. 409–418, Mar. 1982.
[8] J. L. Volakis, T. Özdemir, and J. Gong, "Hybrid finite element methodologies for antennas and scattering," *IEEE Trans. Antennas Propagat.*, vol. 45, pp. 493–507, Mar. 1997.
[9] J. Gong, J. L. Volakis, and H. T. G. Wang, "Efficient finite element simulation of slot antennas using prismatic elements," *Radio Sci.*, vol. 31, no. 6, pp. 1837–1844, 1996.
[10] T. Özdemir and J. L. Volakis, "Triangular prisms for edge-based vector finite-element analysis of conformal antennas," *IEEE Trans. Antennas Propagat.*, vol. 45, pp. 788–797, May 1997.
[11] S. S. Bindiganavale and J. L. Volakis, "Guidelines for using the fast multipole method to calculate the RCS of large objects," *Microwave Opt. Technol. Lett.*, vol. 11, no. 4, pp. 190–194, 1996.
[12] A. C. Polycarpou, M. R. Lyons, J. Aberle, and C. A. Balanis, "Analysis of arbitrary shaped cavity-backed patch antennas using a hybritization of the finite element and spectral domain methods," in *IEEE Int. Symp. Antennas Propagat. Dig.*, Baltimore, MD, July 1996, pp. 130–133.
[13] N. N. Bojarski, "k-space formulation of the electromagnetic scattering problem," Tech. Rep. AFAL-TR-71-5, U.S. Air Force, Mar. 1971.
[14] T. K. Sarkar, E. Arvas, and S. M. Rao, "Application of FFT and the conjugate gradient method for the solution of electromagnetic radiation from electrically large and small conducting bodies," *IEEE Trans. Antennas Propagat.*, vol. AP-34, pp. 635–640, May 1986.
[15] J. L. Volakis and K. Barkeshli, "Applications of the conjugate gradient {FFT} method to radiation and scattering," T. K. Sarkar, Ed., in *Application of the Conjugate Gradient Method to Electromagnetics and Signal Analysis*. New York: Elsevier, 1991, ch. 6.
[16] J. Gong, J. L. Volakis, and A. C. Woo, "A hybrid finite element-boundary integral method for the analysis of cavity-backed antennas of arbitrary shape," *IEEE Trans. Antennas Propagat.*, vol. 42, pp. 1233–1242, Sept. 1994.
[17] C. Y. Shen, K. J. Glover, M. I. Sancer, and A. D. Varvatsis, "The discrete Fourier transform method of solving differential integral equations in scattering theory," *IEEE Trans. Antennas Propagat.*, vol. 37, pp. 1032–1049, Aug. 1989.

Sunil S. Bindiganavale was born on November 12, 1968, in Bangalore, Karnataka, India. He received the B.E. degree (with distinction) in electronics and communication engineering from the Regional Engineering College (REC), Karnataka, India, in 1990, and the M.S. and Ph.D. degrees in electrical engineering from the University of Michigan (radiation laboratory), Ann Arbor, in 1992 and 1997, respectively.

In 1990, he worked on software development for Tata Consultancy Services (TCS), Madras, India. He was a Research Assistant at the Radiation Laboratory from 1991 to 1997. Since August 1997, he has been an Engineering Specialist with the Electromagnetic Analysis and Code Development Group, Northrop Grumman Corporation, Pico Rivera, CA, working on electromagnetics code development on massively parallel computing platforms. His research interests are mainly in the fields of numerical and analytical techniques for applied electromagnetics, with an emphasis on fast algorithms for hybrid numerical techniques.

Dr. Bindiganavale was a recipient of a merit scholarship from the Government of Karnataka for the entire duration of his undergraduate studies as well as an award from the university for finishing second in a class of 200 in the Electronics and Communication Engineering Division.

John L. Volakis (S'77–M'82–SM'89–F'96) was born on May 13, 1956 in Chios, Greece. He received the B.E. degree *summa cum laude* from Youngstown State University, Youngstown, OH, in 1978, and the M.S. and the Ph.D. degrees from the Ohio State Univesity, Columbus, OH, in 1979 and 1982, respectively.

He has been with the University of Michigan, Ann Arbor, MI, since 1984, where he is now a Professor in the Department of Electrical Engineering and Computer Science (EECS). From 1982 to 1984 he was with Rockwell International, Aircraft Division, and from 1978 to 1982 he was a Graduate Research Associate at the Ohio State University ElectroScience Laboratory, Columbus. He has published about 140 articles in major refereed journal articles, more than 140 conference papers, several book chapters on numerical methods, and coauthored two books—*Approximate Boundary Conditions in Electromagnetics* (New York: IEEE Press, 1995) and *Finite Element Method for Electromagnetics* (New York: IEEE Press, 1998). He was an Associate Editor for *Radio Science* from 1994 to 1997. He now serves as associate editor for the *Journal of Electromagnetic Waves and Applications* and the *IEEE Antennas and Propagation Society Magazine*. Along with his students, he develops prototype algorithms for modeling antennas, radar scattering and imaging of aircraft structures and microwave circuits. His primary research deals with the development and application of analytical and numerical techniques to large scale scattering, printed antennas and bioelectromagnetics.

Dr. Volakis received the University of Michigan College of Engineering Research Excellence Award in 1998. He served as an Associate Editor of the IEEE TRANSACTIONS ON ANTENNAS AND PROPAGATION from 1988 to 1992. He chaired the 1993 IEEE Antennas and Propagation Society Symposium and Radio Science Meeting and is a current member of the AdCom for the IEEE Antennas and Propagation Society. He is a member of Sigma Xi, Tau Beta Pi, Phi Kappa Phi, and Commission B of URSI.

Hristos Anastassiu (S'89–M'96), photograph and biography not available at the time of publication.